Wind stress and ENSO dynamics

Hendrik Beijeman

January 14, 2014

Abstract

Recent studies indicate that coupled general circulation models (GCM) display mixed success in simulating the properties of the El Niño/Southern Oscillation (ENSO). Specifically, aggregate runs of various GCMs typically show spatial and temporal disparities compared to observations. We turn to the Zebiak-Cane model of intermediate complexity for the tropical Pacific ocean to study the response of the sea surface temperature (SST) and inter-annual variability of ENSO under different wind stress conditions. Spatial variation is modeled after the meridional structure of the zonal wind stress based on TAO/TRITON measurements, and furthermore on reconstructed Pliocene conditions from the HadCM3 PlioMIP Exp 2 wind data. Temporal variations are introduced with a simple seasonal cycle. Among all conditions simulated, only very weak trade winds result in a "permanent" El Niño with weak SST gradients and no variability. A cold tongue (CT) structure is always present when the wind is above a minimum critical value, although the oscillations vanish if the wind crosses a threshold maximum value. Apart from these extremes, periods of $3 \sim 4$ years are found with ΔSST amplitudes of $5°\text{C} \sim 9°\text{C}$.

1   Introduction

Ever since Jacob Bjerknes suggested in 1969 that the El Niño phenomenon is the oceanic expression of a complex ocean-atmosphere interaction the subject has been the focus of intense study. Today, El Niño and its counterpart La Niña are colloquially known as ENSO, or the El Niño Southern Oscillation.

The relatively large equatorial Pacific basin allows for unobstructed ocean currents and atmospheric winds. The sea surface temperature (SST) gradients force the atmospheric circulation over the ocean and in turn, the winds force the upper layer ocean currents. In the equatorial Pacific, the winds are predominantly easterly, and hence cause a pile up of warm surface waters in the west near Indonesia. In response there is significant upwelling in the eastern part of the basin, resulting in large pool of cold water. This large zonal SST gradient causes a strong atmospheric circulation, known as the Walker Circulation. In this coupled picture there also exist many dynamical modes, of which ENSO is the strongest. The periodic discharge of the latent ocean heat in the west causes a sudden reversal with strongly heated conditions in the east.

It is one of the most interesting naturally occurring climate variabilities known because of its strongly confined spatial extent and well defined temporal characteristics, recurring roughly every 3 to 4 years. In addition, the local variations in climate caused by ENSO can be easily measured, and do not need careful application of advanced statistical methods to be resolved.

1.1   The global picture

There is a global significance to ENSO. During the El Niño phase the cold pool is much warmer than normal, sometimes by as much as 5°C during extreme events. Extensive convection creates thunderstorms and increased rainfall across the South American coast, causing major flooding whenever the event is strong. The ocean upwelling transports essential nutrients for large fish populations off the coast of Ecuador and a reduction in upwelling immediately affects the dependent ecosystem. The warm phase with reduced upwelling usually happens in December, and the Peruvian fishermen called the disappearance of fish around Christmas time "El Niño ", or the "Christ Child".

The effects of El Niño are not constrained to the Americas. Many millions of people around the globe are directly affected by its effects. In large parts of Africa the weather will be wetter and colder than usual, whereas in East Asia and Western Australia conditions will be drier with consequences for bush fires and haze. There are even weak teleconnections to Europe [1]. Likewise, a strong La Niña will cause mostly the reverse effects for the affected regions globally.

There are three routes available to study the ENSO phenomena. Along the first theoretical route has emerged two simple pictures of the physics behind ENSO ([9]) as a *delayed oscillator* and as a *recharge oscillator*. In the latter model, ENSO is represented as a classical damped oscillator, with the SST and thermocline playing the role of momentum and position, respectively. Although this model has surprisingly good qualitative agreement with observations, it is still lacking as a prediction tool due to its severe oversimplification of the ocean-

---

[1]See http://www.knmi.nl/research/global_climate/enso/effects/ for details

atmosphere interaction and seasonal cycle. The second route is by studying a numerical *Intermediate Complexity Model* (ICM) that models the basin itself and imposes simple but realistic boundary conditions. Fully coupled ICMs are capable of showing much of the dynamic behavior of ENSO modes, and accurately reflect the mean state climatology of the region in the SST, surface winds, and thermocline depth. ICMs are also quite suited to investigate the effects of the various feedbacks present in the system. The relative computational simplicity of ICMs comes at a cost however. Outside influences must be modeled or ignored, for example, in the case of the ICM used in this thesis, the wind stress is composed of an external component due to the Hadley circulation which itself is not modeled but prescribed in an ad-hoc fashion.

To retain all information on the feedbacks, a global, fully coupled 3D Ocean-Atmosphere model must be used. These Global Climate Models (GCMs) are also vitally important tools to study the effects of increased greenhouse gases on the climate and the future behavior of ENSO.

1.2 Research question

In a recent study with an ensemble of 22 different state-of-the-art GCMs running CO_2 doubling experiments [8]the effects of global warming on the equatorial Pacific was investigated. The emerging picture is very complex, but in general, the equatorial Pacific will experience enhanced warming, with SST spatial signatures resembling El Niño like events. In the simulations, the equatorial warming of the SST was concentrated farther west than is actually observed. This west-ward shift is also seen in the position of the cold tongue and in the concentration of warm waters during El Niño events. Only 3 out of the 22 models showed unambiguous El Niño -like SST responses with realistic temporal and spatial characteristics. Comparable results were obtained in runs of 21 different IPCC AR4 coupled GCMs ([17]). Although it is still unclear why the GCMs struggle to reproduce a realistic ENSO, the Zebiak-Cane type ICMs do very well in that regard.

The original Zebiak-Cane model was used in conjunction with a historically accurate background climatology ([16]), and was used to calculate anomalies on this background state. Later ICM studies have examined the effect of various model parameters on the characteristic ENSO mode while also generating a mean-state climatology (see [1], [2], [3]), making them truly self-contained.

In light of the results of recent GCM runs, it is interesting to return to the latter ICM and study the influence of a spatially and temporally varying external wind stress on the position of the Cold Tongue and on the amplitude and period of the ENSO mode. The first approach is to investigate the realistic range of variability in wind stress in the model used by Dijkstra et al ([2]), which allows varying the strength of the equatorial maximum and off-equatorial maximum wind stress. Next, actual mean wind fields from the TAO/TRITON array are modeled and input in the ICM, and compared with the reference case. Another avenue is to isolate and model the seasonal variations present in the TAO/TRITON wind fields. Finally, reconstructed wind fields from the Pliocene era are investigated for the existence of a "permanent" El Niño state ([1])
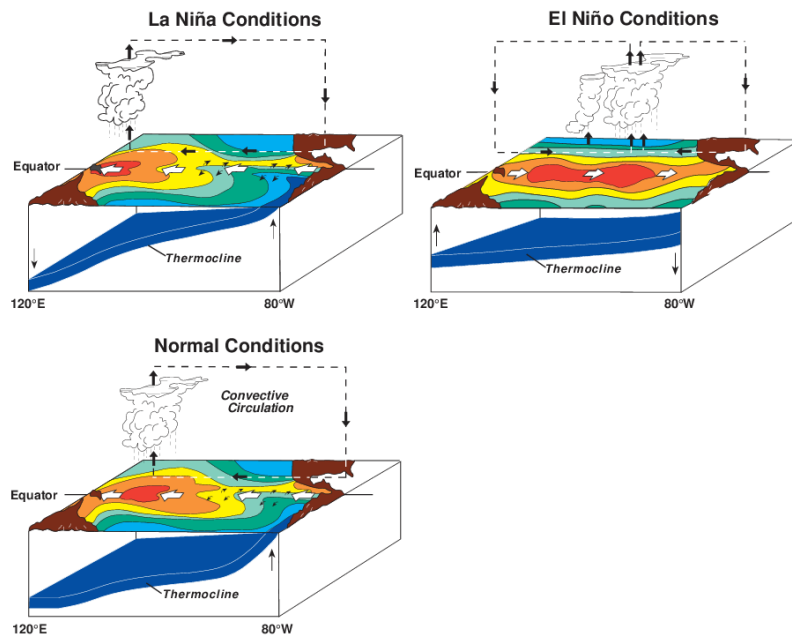
Figure 1: The three common states of ENSO. During normal conditions, the Walker circulation transports moist air from East to West, where the air will rise and cause precipitation over the warmer western waters over Indonesia and eastern Australia. The induced wind stress causes upwelling of colder waters in the east, raising the thermocline there. During El Niño conditions the pool of warm water flows back east, causing significantly warmer sea-surface temperatures, a flattening of the thermocline blocking upwelling, and a collapse of the Walker circulation. In contradistinction, La Niña conditions show a steeper thermocline than normal, resulting in stronger upwelling and hence cooler sea-surface temperature. The strong gradient of SST during La Niña enhances the Walker circulation and changes the precipitation patterns.
Credit: TAO Project Office/NOAA/PMEL

2 The Zebiak-Cane model

The model used is a variation of the original Zebiak-Cane model [16], the first fully coupled model of the equatorial ocean-atmosphere interaction. Originally, it coupled a Gill atmosphere to a shallow water ocean anomaly model that works on external temperature and wind data. [3] extended the model to generate a full climatology on its own.

2.1 The Gill atmosphere

In his 1980 seminal paper, Gill proposed [4] a computationally effective model to study the response of the tropical atmosphere under diabatic heating. By expanding the heating in normal modes (in the form of parabolic cylinder functions) he analytically demonstrated that the equatorial symmetric heating distribution gives rise to the Walker Circulation (see [5]), while the asymmetric part is the dominant contribution to the meridional circulation.

Gill's atmospheric model is that of an incompressible fluid in a box with a lid, with a prescribed zonal length L and of infinite meridional extent. This latter seemingly artificial requirement is solely for the purpose of making use of the orthogonality properties of the Hermite functions to facilitate the analytical solutions, and is of no consequence to our numerical model.

The horizontal versus vertical scale warrant the use of the shallow water equations. In non-dimensional form these are,

$$\epsilon u_a - \frac{1}{2} y v_a = -\frac{\partial p_a}{\partial x} \tag{1a}$$

$$\epsilon v_a + \frac{1}{2} y u_a = -\frac{\partial p_a}{\partial y} \tag{1b}$$

$$\epsilon p_a + \frac{\partial u_a}{\partial x} + \frac{\partial v_a}{\partial y} = -Q \tag{1c}$$

$$w_a - \epsilon p_a = Q \tag{1d}$$

u_a, v_a, w_a represent the wind velocities, p_a the pressure, and Q the external heating. In these equations the linear damping term ϵ is introduced by imposing a Rayleigh-type friction by replacing the operator $\partial/\partial t$ by $\partial/\partial t + \epsilon$ and seeking steady-state solutions. [2]

A weakness in this model is the rather ad-hoc use of the forcing Q. In some fashion this forcing must be related to the SST, and the simplest interpretation is to presume Q to be proportional to the SST. Lindzen and Nigam 1987 proposed a more complete parameterization of Q using moisture and back-pressure. However, Neelin demonstrated in [6] that this results in the same set of equations as Gill, except with a different characteristic length scales. In the model a linear parameterization of Q is used,

$$Q(T) = \alpha_T (T - T_0) \tag{2}$$

where T is the ocean surface temperature (SST) and T_0 the radiative equilibrium temperature.

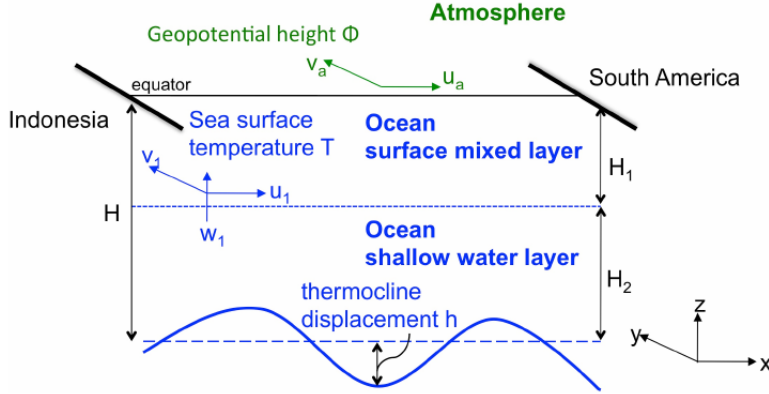[2]The time evolution is implicit later on in the coupling to the oceanic model through Q.

Figure 2: Schematic representation of the Zebiak-Cane model. The ocean model consists of a surface mixed layer of depth H_1, on top of a shallow water layer with depth $H - H_1$. The thermocline marks the separation between the motionless deep ocean. The atmospheric motions are given by the horizontal velocities u_a, v_a, while the mixed layer ocean velocities given by u_1, v_1, w_1, the latter determining the upwelling of colder water. Zonally, the ocean is bounded by the continents at Indonesia in the east, and South America in the west, and is presumed to extent infinitely in the meridional direction.
Figure taken from [1].

2.2 The coupled ocean component

The ocean model is reduced gravity shallow water model[3]. In this model the ocean is assumed to consist of an upper layer with density ρ and depth H, situated above the motionless deep ocean with density $\rho + \Delta\rho$. On the equator the β-plane describes the Coriolis dynamics, and the momentum equations become,

$$\frac{\partial u}{\partial t} + a_m u - \beta_0 y v + g' \frac{\partial h}{\partial x} = \frac{\tau^x}{\rho H} \tag{3a}$$

$$\beta_0 y u + g' \frac{\partial h}{\partial y} = \frac{\tau^y}{\rho H} \tag{3b}$$

In equation 3b the long wave limit is taken and the acceleration of the meridional velocity v can be neglected. The momentum balance is amended by the constraint of continuity,

$$\frac{\partial h}{\partial t} + a_m h + c_o^2 \left(\frac{\partial u}{\partial x} + \frac{\partial v}{\partial y} \right) = 0 \tag{4}$$

The surface velocities are the Ekman layer velocities,

$$a_s u_s - \beta_0 y v_s = \frac{H_2}{H} \frac{\tau^x}{\rho H_1} \tag{5a}$$

$$a_s v_s - \beta_0 y u_s = \frac{H_2}{H} \frac{\tau^y}{\rho H_1} \tag{5b}$$

---

[3]See appendix A for an overview

This provides one path of the coupling through the wind stress $\vec{\tau}$, which in the model is assumed to be linearly related to the atmospheric wind, i.e. $\vec{\tau} = \gamma \vec{v_a}$. [4]. The wind stress is thought to be composed by an internally generated contribution $\vec{\tau_c}$ and an external component $\vec{\tau_{ext}}$. The external wind stress is prescribed and thought to arise due to influences outside of the model described here. In particular, the external wind stress is identified with the equatorial convergence of the surface winds due to the Hadley cells. In the reference model the external wind stress is assumed to be prescribed by,

$$\tau_{ext}^x = \tau_0 \left(F_0 + F_1 y^2 \right) e^{-y^2/2L_a^2} \tag{6a}$$
$$\tau_{ext}^y = 0 \tag{6b}$$

where τ_0 is a constant with dimension Pa and F_0, F_1 are dimensionless constants[5]. The scale L_a is taken to be the typical value of the atmospheric Rossby deformation radius. Typical values for τ_{ext}^x are $\sim 0.02\ Pa$.

2.3 Boundary conditions

The basin is assumed to extent to infinity in the meridional direction where the sea velocities are zero. In the zonal direction there are rigid boundaries at $x = 0$ and $x = L$, with $L = 15000$km. These boundaries reflect the continental geometries of Indonesia and South-America respectively. There is momentum exchange between the Pacific ocean and the Indian ocean at $x = 0$, but the mass transport must be balanced. At the eastern boundary at $x = L$ lies the rigid coastal boundary of the American continent, and the flow cannot cross this boundary. Hence, the boundary conditions become,

$$u(L, y, t) = 0 \tag{7a}$$
$$\int_{-\infty}^{\infty} u(0, y, t)\, dy = 0 \tag{7b}$$
$$T(0, y, t) = T_0 \tag{7c}$$

2.4 Thermocline model

To complete the coupling something must be said about the temperature evolution of the sea surface. The sea surface temperature equation is,

$$\frac{\partial T}{\partial t} + a_T(T - T_0) + \frac{w_1}{H_1}\mathcal{H}(T - T_s(h)) + u_1 \frac{\partial T}{\partial x} + v_1 \frac{\partial T}{\partial y} \tag{8a}$$
$$u_1 = u_s + u \tag{8b}$$
$$v_1 = v_s + v \tag{8c}$$
$$w_1 = w_s + w \tag{8d}$$

where u_1, v_1 are the horizontal velocities in the mixed layer, and w_1 is the vertical velocity just below the mixed layer, and $T_s(h)$ the subsurface sea temperature.

---

[4]This linearization can be motivated for small values of $\vec{u_a}$. However, a more realistic approach is used in section 3.2

[5]Strictly speaking F_1 has dimensions m^{-2}, but the numerical model uses a dimensionless y-coordinate.

$T_s(h)$ is assumed to be parameterized by,

$$T_s(h) = T_{s,0} + (T_0 - T_{s,0}) \tanh\left(\frac{h + h_0}{H^*}\right) \qquad (9)$$

This parameterization regulates T_s between $T_{s,0}$, the characteristic subsurface temperature, and the equilibrium T_0. The constants h_0 and H^* control the steepness and offset of the vertical structure. Summarized, the external wind induces sea surface motion. Sea surface motion causes a change in the SST through $T_s(h)$, and changes in T again causes changes in the surface winds.

2.5   The Delayed Oscillator

At first, the external easterlies will cause upwelling of cooler water across the equator. The resulting gradient in SST will in turn generate an internal wind that causes yet more upwelling, which in turn amplifies the gradient in a positive feedback. The boundary conditions on the domain reflect the geometry of the geography. In particular, the eastern boundary has a no-flow condition due to the presence of the American coast. This natural barrier causes a concentration of cold water in the east, resulting in the cold tongue. The upwelling of cold water in the east causes a sloping of the thermocline bringing it closer to the surface. In the western part of the basin the warm water accumulates, and increases the depth of the thermocline. An enhanced CT is indicative of a La Niña state, whereas a reduced CT with warmer waters in the east is called the El Niño state. This latter scenario can happen for example when the easterly trades weaken allowing the warm pool of water in the west to flow back east. It is not obvious why one (permanent) state should be preferred to the other, or why the ocean in fact flips between these two states. It was not until the late 1980s that a theoretical framework was developed to understand the mechanism of oscillation, coined the *delayed oscillator* theory.

In this model [14], the SST evolution $(T(t))$ is assumed to be determined by the following dimensionless delay equation,

$$\frac{\mathrm{d}}{\mathrm{d}}T(t) = T(t) - T(t)^3 - AT(t - \Delta) \qquad (10)$$

Changes in the thermocline cause oceanic Rossby waves, located to the north and south of the equator, to move across the basin from east to west. These waves ultimately reflect off the western boundary and become east-ward traveling equatorial Kelvin waves. These Kelvin waves lower the thermocline in the west and central part of the basin, increasing the SST locally and reducing the induced winds over the weakened SST gradient. This warming will then reach a maximum at some point. Eventually the external wind will cause upwelling again and start the cycle anew.

The delayed part (the A term in eqn 2.5) has its roots in the observation that a warm SST perturbation causes a deepening of the thermocline and also a westerly perturbation in the wind. This will result in the creation of Rossby waves that will arrive after a delay (reflection off the western boundary) to counteract the warming SST through upwelling.

3   Results

3.1   Reference output

The model output of subsequent runs is compared against the results of the reference output. The reference is taken from [1] and has the following operational parameters,

Geometry		
n_x	29	x-grid size
n_y	30	y-grid size
L	1.5×10^7 m	zonal extent
L_x	$L/n_x = 5.2 \times 10^5$ m	zonal cell size
L_y	$\sqrt{c_o/\beta_0} = 3.0 \times 10^5$ m	meridional cell size
H	200 m	ocean layer depth
H_1	50 m	ocean surface layer depth
Temporal		
c_o	$2\ m/s$	oceanic Rossby wave propagation speed
c_a	$30\ m/s$	atmospheric Rossby wave propagation speed
t_s	$L/c_o = 3.0 \times 10^7 s$	Time interval per integration step
n_t	270	Number of time steps

The most important feature of this reference point is the shape of the external wind stress. Recall that it is assumed that this wind stress originates from mechanisms outside the influence of simulation domain. One such mechanism is the surface zonal wind convergence due to the Hadley circulation. The external wind stress is assumed to be static, zonal, and of decreasing strength away from the equator. In the reference case a Gaussian profile is chosen both for convenience and to facilitate mathematical analysis of the model equations.

The numerical integration is terminated after 270 steps, corresponding roughly to 24 years. At the onset of the integration the whole ocean is in radiative equilibrium with temperature T_0. Immediately after this, the upwelling causes a formation of the CT, and, depending on the strength of the external wind stress, a sustained oscillation (with the ENSO mode) or rather a permanent CT (also called *permanent El Niño state*) if the wind stress is too weak or too strong.

The external wind stress in the reference case is prescribed by eqn. 6. In the reference case, the external wind is fully characterized by the non-dimensional parameters F_0, F_1, and has the values $F_0 = 0.2$ and $F_1 = 0$, corresponding to a maximum external wind stress of $\tau_x \approx 0.002\ Pa$ on the equator, or, a wind speed of $u_a \approx 1.5 m/s$.

Figure 3 shows the mean-state climatology of the reference output. The most prominent features are the strong CT with a central temperature of $26°C$ and the ENSO mode with an amplitude of $6°C$ and a period of 3.5 years. When the external wind weakens or even seizes altogether (c.f. figure 4), the warm pool of water quickly discharges and the ocean soon restores radiative equilibrium. One particular strong oscillation can be seen in figure 5. The thermocline in the western part of the basin (box (b)) is deepening while it is much closer to the surface in the east (box(a)), especially during the La Niña phase.

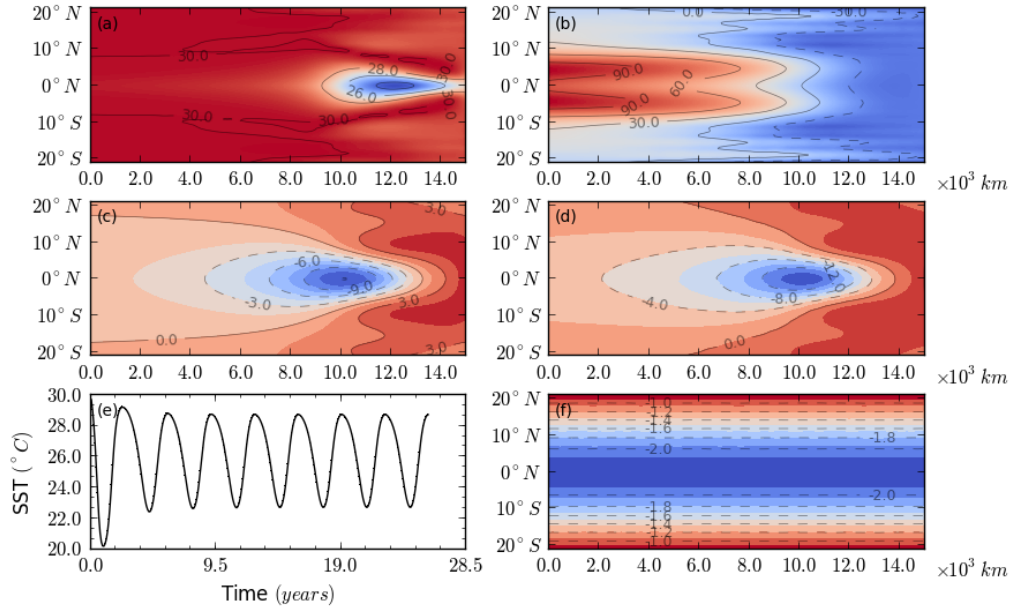The spatial variations during one cycle of the oscillation in the SST, ther-

Figure 3: The reference output mean climatology: (a) The sea-surface temperature (°C) (b) The thermocline depth anomaly compared to a fixed reference level (m) (c) The induced zonal wind speed (m/s) (d) The total zonal wind stress (mPa) (e) Time series of the SST in the *NINO3* region. (f) The external zonal wind stress (mPa)

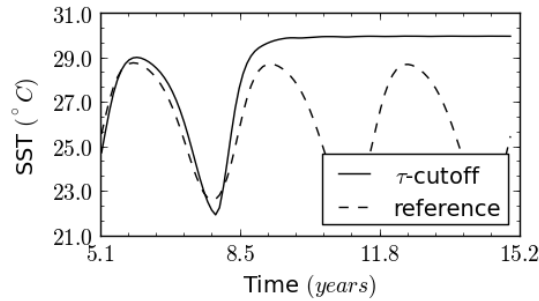Figure 4: Comparison of sustained easterly trades with weakening trades (τ-cutoff). The external wind collapses in the τ-cutoff sequence shortly before the 8.5 year mark, at the height of the La Niña phase. The ocean restores quickly to original radiative equilibrium after a couple of months.

mocline (TCD), and induced wind can be seen in figures 18, 19 and 20. The starting point is the top left panel, showing the moment in time when the ocean assumes its mean state surface temperature. Time proceeds in the lower panels with equally spaced temporal intervals.

Even when the SST is in its mean state, it can be seen in 19.(a) that Rossby waves are already forming in the north-east and south-east parts of the basin
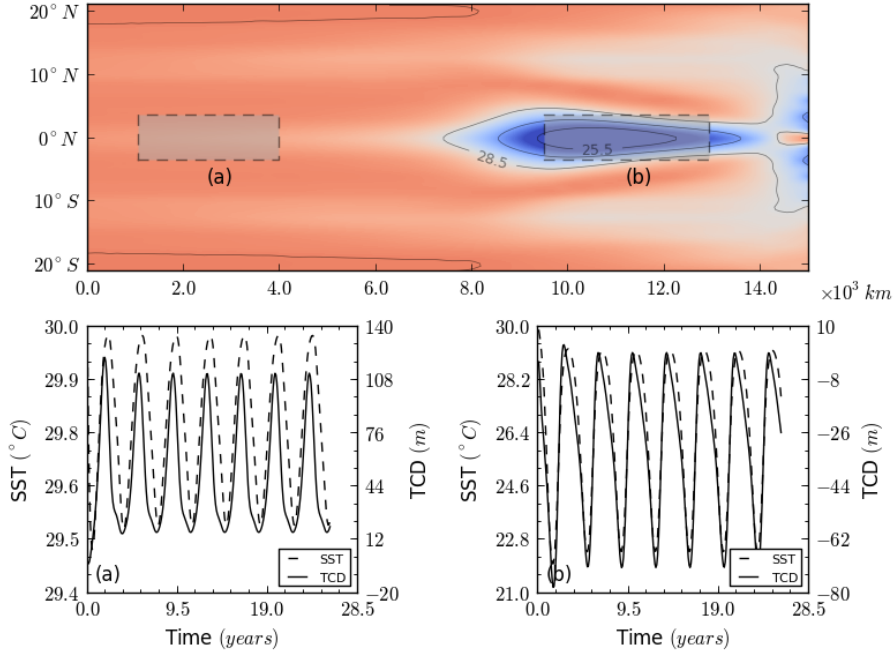
Figure 5: Time series of the SST and thermocline depth anomaly (TCD) for $(F_0, F_1) = (0, 0.04)$. The plotted values are the spatial mean of the SST and TCD in boxes (a) and (b). Box (b) roughly corresponds to the *NINO3* area for measuring SST anomaly values. The top plot shows the mean state SST.

where the thermocline lies close to the surface. Halfway through the cycle a Kelvin wave can be seen to start to travel to the east in 19.(e). The sea surface temperature reacts to the tilting of the thermocline, and reaches the peak of the El Niño phase in panel 18.(c) when the waters are generally warmest. Indeed, half a cycle later in panel 18.(f) the SST reacts to the passing of the Kelvin wave with the formation of a strong CT (La Niña phase).

During the peak of the El Niño phase, the trades have virtually collapsed due to the westward blowing external wind, and the eastward blowing induced wind. This is clear in panel 20.(c). In contradistinction the external wind is amplified by the induced wind during the peak of the La Niña phase in panel 20.(g).

Clearly the model is remarkably effective in demonstrating the core features of the natural El Niño cycle.

3.2   Off-equatorial maximum wind-stress

The reference case has an external wind stress form prescribed by eqns 6. The reference output has values $(F_0, F_1) = (0.2, 0)$, which has a global maximum wind stress on the equator.

In general there is either one global equatorial maximum, or two local maxima located at $y \in (0, y_\pm)$ with $y_\pm = \pm \Re(\sqrt{2L_a^2 - F_0/F_1})$. The condition for the existence of an off-equatorial maximum is that $F_1 > F_0/2L_a^2$, and for smaller

values the solutions are expected to mimic those of the reference model with $F_1 = 0$ but with larger L_a and F_0. The greatest distance of the local maximum is at $y_\pm = \pm L_a\sqrt{2}$ with wind stress $\tau_{\text{ext}}^x \approx L_a^2 F_1 \tau_0$.
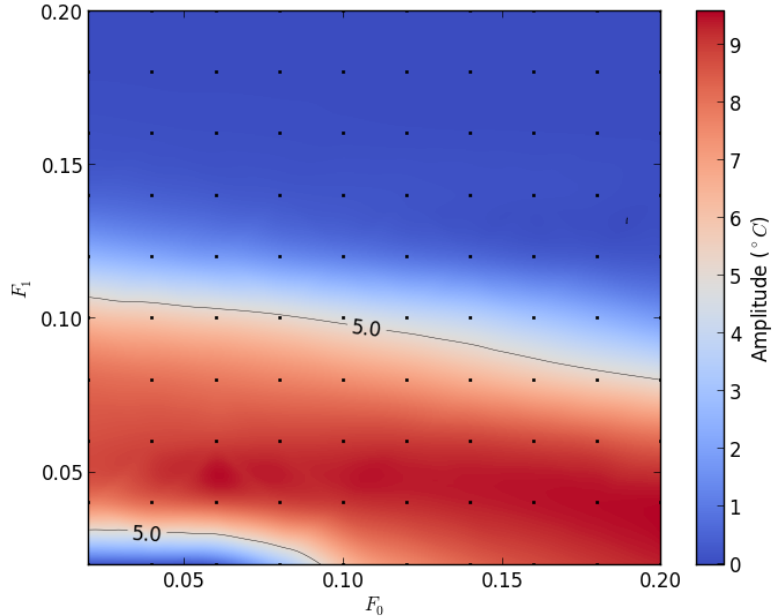

Figure 6: Maximum ΔSST for the parameter space spanned by (F_0, F_1). The two solid lines indicate the boundary in F_0, F_1 space where stable oscillations occur. Values below 5°C amplitude typically show no or decaying oscillations. Moving along the F_0-axis the oscillations can be seen to vanish below $F_0 = 0.08$. This is a critical value of τ_{ext}^x below which no oscillations can be sustained (the Hopf-bifurcation point, see [2]). Likewise, for too high values of τ_{ext}^x the oscillations also disappear due to over driving. The black dots indicate the individual integration runs. For $F_1 > 0.025$ the wind stress has two off-equatorial maxima.

A number of integrations were run within the parameter range $F_0, F_1 \in (0, 0.2)$. For values $F_1 = 0, F_0 < 0.08$ no oscillations exist (c.f. figure 6). Above this point the oscillations quickly build up in strength to reach a local maximum in the red island around $F_1 = 0.05$ and $0.08 < F_0 < 0.2$. The special point marking the onset of oscillatory behavior corresponds to the Hopf-bifurcation point as discussed in [2]. For values of $F_0 > 0.5$ (not shown) the integration results become unphysical as the thermocline modeling breaks down.

Near the F_0-axis in figure 6 there is only a single global equatorial maximum in the wind stress, but above the horizontal line $F_1 = 0.025$ the maximum splits into two off-equatorial maxima as described earlier. Furthermore, along the F_1 axis there is no equatorial wind stress at all.

From the results it appears to be easier to excite Rossby waves with an off-equatorial weak wind maximum. In fact, in the extreme situation where there is no equatorial wind stress (along the F_1 axis) it is quite easy to trigger oscillatory behavior. In the case of a pure equatorial maximum a stronger wind is required to generate the oscillations.
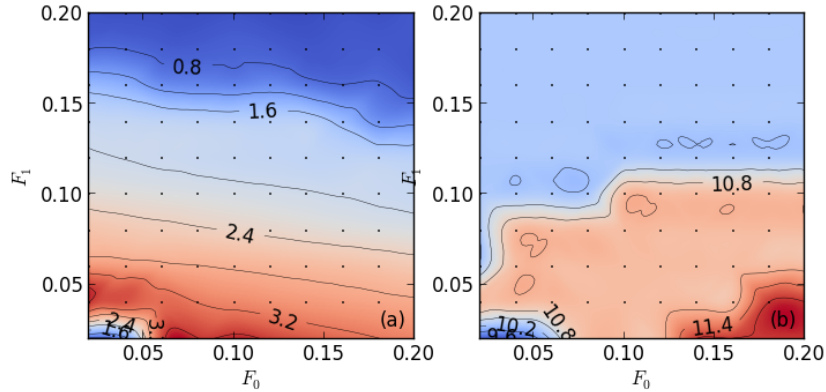
Figure 7: Variability of the period of oscillations and the position of the CT in F_0, F_1 space. (a) Period of the oscillation in years. Decaying oscillations have a lower period than sustained oscillations, with periods of a few months up to about 2.4 years. Sustained and stronger oscillations typically have periods of 3 to 4 years. (b) Eastward position of the Cold Tongue, in 10^3 km. The position of the CT shows little dependence on the period or amplitude of the oscillations. However, there is a slight eastward movement of the CT associated with stronger easterlies near the equator.

All oscillations in F_0, F_1 space exhibit remarkable similarity. When the wind-stress is below the threshold value, the initial oscillations are damped to extinction. Too large a wind-stress, and the initial oscillations form a deep CT and then dampen out. In between exist a broad region in F_0, F_1-space where very regular oscillations occur with periods ranging from 2 to 4 years, and with amplitudes between 2°C and 10 °C . Figure 7 shows the variations in the period of the oscillation and the (equatorial) position of the CT in F_0, F_1-space. In panel 7.(a) stable oscillations exist below the line 2.4 years. When the wind stress is weak (lower left corner), the period is smaller than 2 years. In the region with stable oscillations, the period varies little and does not appear to depend on the spatial variation of the external wind stress. Panel 7.(b) shows the variation of the position of the CT in F_0, F_1-space, as measured by the location of the global minimum SST in the mean-state. The units are in 10^3 km, as measured from the western boundary. The CT location has negligible variation with the strength of the wind stress.

The regularity of the ENSO mode exhibited in this model suggests that there exists a closed trajectory in (SST,TCD) space, and indeed, for stable oscillations there exists such a unique trajectory (c.f. figure 8). Panel 8.(a) shows the trajectories of the aggregate phase space of all the runs from F_0, F_1-space. All trajectories were sampled after 10 years from the beginning of the integration. The SST and TCD are the spatial mean of the *NINO3* box defined earlier in 5.(a). Oscillations that do not develop due to weak wind stress stay on fixed points in the upper right part of the panel (high SST, high TCD). The stable oscillations (like 8.(c)) occupy the horizontal band, while the decaying oscillations due to over-stressing can be discerned as the parallel horizontal bands in the lower left panel. 8.(b) shows a single such decaying oscillation.
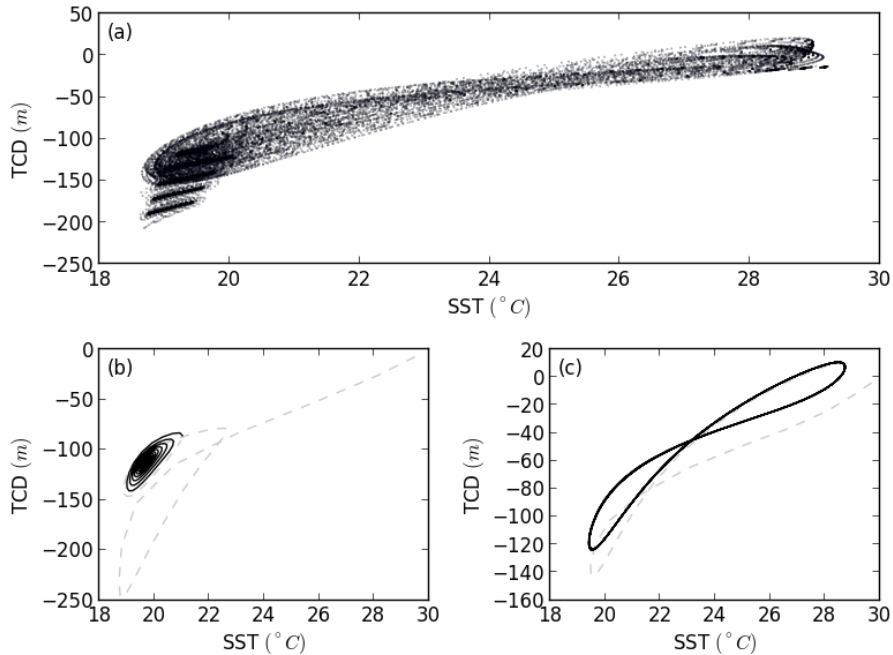
Figure 8: Phase diagram of the ENSO mode. Diagram (a) shows the aggregate phase space of 20 runs with different F_0, F_1 parameters. When the zonal wind is too strong, the oscillation quickly decays (b), and a static CT forms. Finally, diagram (c) shows a fully developed oscillation. The closed orbit demonstrates the regularity of the oscillation. The dashed line shows the initial behavior starting at $t = 0$ with values $TCD = 0m$ and $SST = 30°C$.

3.3   TAO/TRITON fit

The 1982-1983 El Niño event came undetected and unpredicted until almost at its peak [10]. This brought home the need for real-time measurements from the tropical Pacific, and construction was started in 1982 on an array of moored buoys distributed across the equator, called the TAO array. In 1994 the full array of 70 buoys was commissioned and later christened the TAO/TRITON array. This array is still in operation today and is supported by a collaboration between the US (NOAA) and Japan (JAMSTEC). A single buoy provides a wide range of near real-time sensor data, including surface wind vectors, sea-surface temperature, and sub-surface temperatures up to about 500m depth. The latter is used to gauge the depth of the thermocline.

Powered by the extensive record of accurate measurements it is interesting to investigate more realistic external wind stress patterns that are better aligned with the wind profile obtained from the TAO/TRITON data.
The external wind stress profile chosen in the reference model has some realistic features, but it nevertheless is arbitrarily chosen. To gain more insight in the model the wind stress will be approximated to observed values for the zonal wind speed.
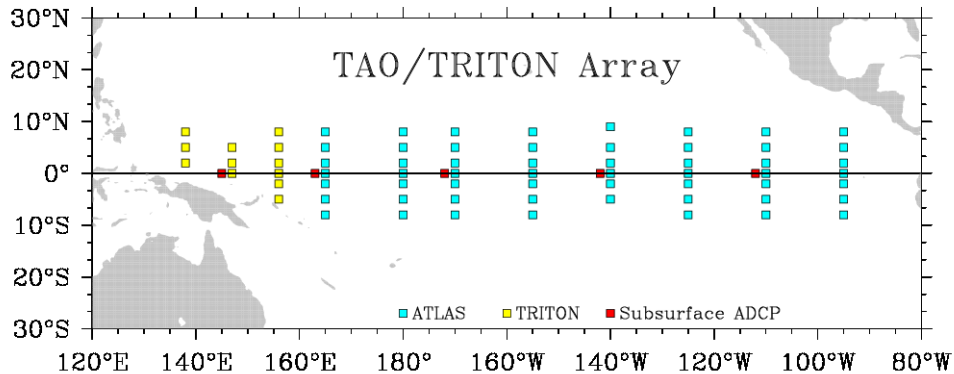
Figure 9: The location of the buoys of the TAO/TRITON array in the equatorial Pacific Ocean
Courtesy of the TAO Project Office/NOAA/PMEL

A major complication is the model's decomposition of the wind stress into a coupled and an external contribution, $\tau = \tau_c + \tau_{\mathbf{ext}}$. The TAO data naturally only provides the wind velocity, and not the (external) wind stress. TAO wind velocity can be translated to a wind-stress using the wind drag relation $\tau = \rho_a C_D v_{10}^2$, where ρ_a is the atmospheric surface density, v_{10} the wind speed at 10m above the surface, and $C_D \approx 1.25 \times 10^{-3}$ the dimensionless wind stress drag coefficient. The value for C_D is taken from [13]. [6] The density of air is assumed to be constant at $\rho_a = 1.15$ kg m^3. Figure 10 shows the mean TAO/Triton zonal wind data, averaged over the years 1989-present. The plot was created by taking the daily averaged data from the 68 TAO/Triton stations as shown in Figure 9. The time-average was taken, and the resulting data points interpolated on a high resolution grid using a generic curvature minimizing algorithm. This record obviously contains the history of many El Niño events, and in the scope of the model, it also contains a fictitious *induced* wind stress and *true* external wind stress.

To extract the external wind stress the pseudo stress field is zonally averaged from 80°W to 140°E resulting in a $\tau_{ext}^x(y)$ that will be input for the model. The presumed benefit of this strategy is that it will average out the induced wind component which has a strong zonal dependence.

Instead of determining the precise external wind contribution to TAO data (if such a thing can be done meaningfully at all), an approximate qualitative fit of the TAO wind is sought and the model output investigated to find numerically corresponding values for the total atmospheric wind. In line with the reference model, the fit is based on the zonally averaged TAO wind profile as in figure (10). The fit to be used is,

$$\tau_{\mathrm{ext}}^x = \tau_0 \left(G_0 e^{-y^2/L_0^2} + G_1 e^{-(y-y_1)^2/L_1^2} \right) \tag{11}$$

---

[6]There are more accurate parameterizations of the wind drag coefficient, see for example [11],[12] and [13]. In general there cannot be given a simple, absolute parameterization, because C_D depends on region, season, and timescale. The constant approximation is sufficient for the current purpose.
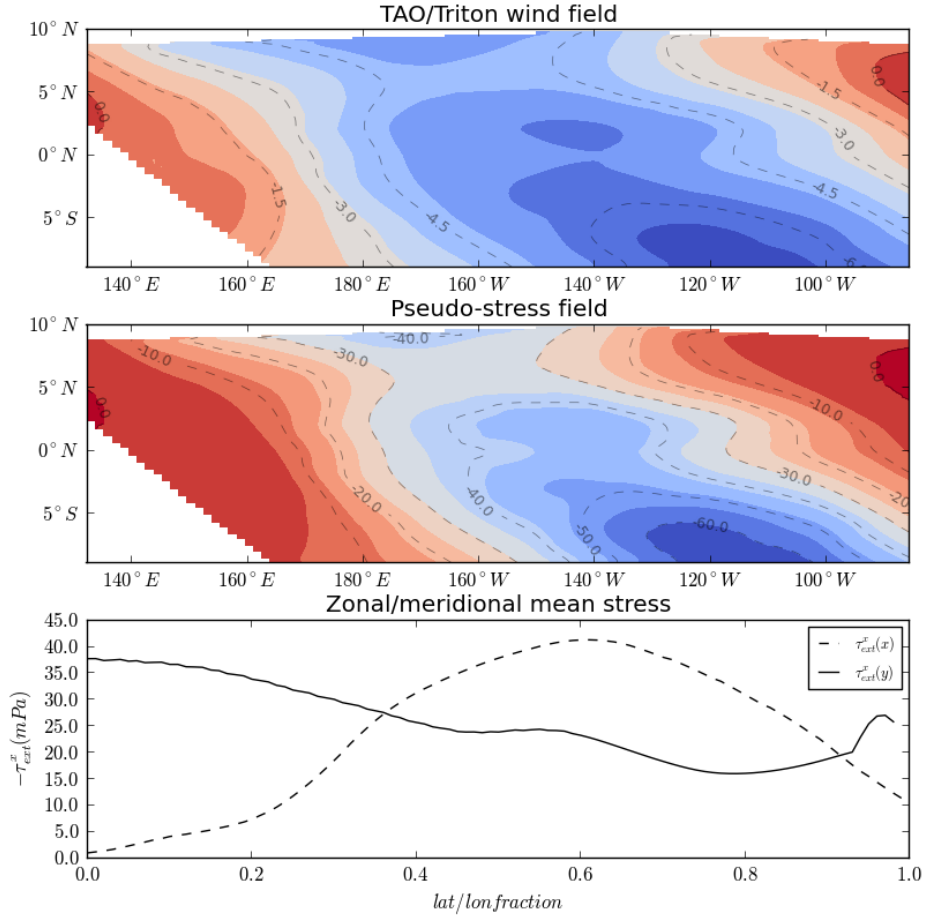
Figure 10: Interpolated mean TAO/Triton zonal wind data averaged over the years 1989-present. The top panel shows the zonal wind component (m/s). The wind is predominantly easterly over the basin, reaching maximum strength around 120°W, 5°S. This area also contains the CT, and the local wind maximum appears roughly 2000km west of the CT, consistent with the reference case (c.f. Figure 3). The TAO data shows the interannual southward position of the ITCZ, as seen from the southern concentration of wind stress. The center panel shows the derived pseudo wind stress (mPa). The bottom panel shows the zonally and meridionally averaged wind stress (solid and dashed curve respectively). The meridional average confirms that the maximum windstress is located around 140°W. The external wind stress is taken to be the zonally averaged $\tau_{ext}^x(y)$ (solid curve) over the whole basin.

with G_0 the free parameter describing the equatorial symmetric wind contribution as in the reference model, and G_1 the off-equatorial local minimum. Notice that G_1 here has the same interpretation as in the reference case, but with a different scaling and units. Finally the constants L_0 and L_1 determine the broadness of the contributions and are tuned to give the approximate shape of the TAO profile. Likewise the local meridional minimum is located at fixed
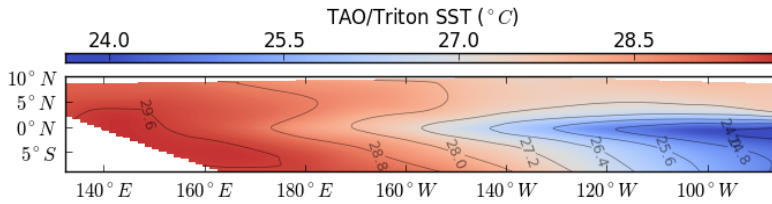
Figure 11: Mean SST in the Pacific basin from the TAO/Triton project from the period 1989-present. The CT is clearly visible to the eastern boundary. It is located further east compared to the reference case (c.f. Figure 3), and slightly south of the equator. This is consistent with the southern position of the ITCZ. In the western part of the basin the SST reaches 30°C , while in the CT it is 24°C . Note that both values are also consistent with the reference case, (where the western SST takes on the value of T_0).

y_1. Compare eqn 11 with the solid curve for $\tau_{ext}^x(y)$ in figure 10, where the G_0 component corresponds to $\tau_{ext}^x(0°N)$ and the G_1 component with $\tau_{ext}^x(10°S)$.

The result of the simulation can be seen in figure 12. The ENSO mode has a slightly longer period of 4.0 years and an amplitude of 5.6°C . The CT is more easterly confined at $x = 12.9 \times 10^3$km compared with $x = 12.3 \times 10^3$km for the reference case.

3.4 Seasonal variation

In the previous section the mean background state was considered, neglecting temporal variations. When inspecting the TAO/TRITON zonal wind data (figure (13)), it becomes apparent that especially the eastern equatorial part of the basin shows a strong seasonal periodicity. As one travels westward the variations become less regular and show less correlation to a seasonal period. The seasonal variations in SST and wind in the tropical Pacific are still poorly understood. To investigate the influence of such a seasonal variation a simple oscillation is added to the external wind stress with a period of 1 year,

$$\tau_{\text{ext}}^x = \tau_0 \left(F_0 + \frac{1}{2}\alpha \left(\cos \omega t - 1 \right) \right) e^{-y^2/2L_a^2} \tag{12}$$

Again the free parameters are F_0 and α. The temporal modulation is chosen in such a way that the maximum wind stress value is determined solely by F_0, and that for $\alpha = 0$ the situation reduces to the reference model. The equatorial maximum wind stress is $\tau_0 F_0$ and minimum $\tau_0(F_0 - \alpha)$.

Figure 14 shows the variations due to different seasonal cycles. The modeled seasonal cycle does not influence the period of the ENSO-mode or one of the other characteristics. Rather, there appears some superficial modulation of the amplitude that is in phase with the seasonal cycle. A different approach must be devised to study the influence of temporal variations in this model. Of particular and ongoing interest is the influence of stochastic processes that can trigger an El Niño when the system is in a critical state.
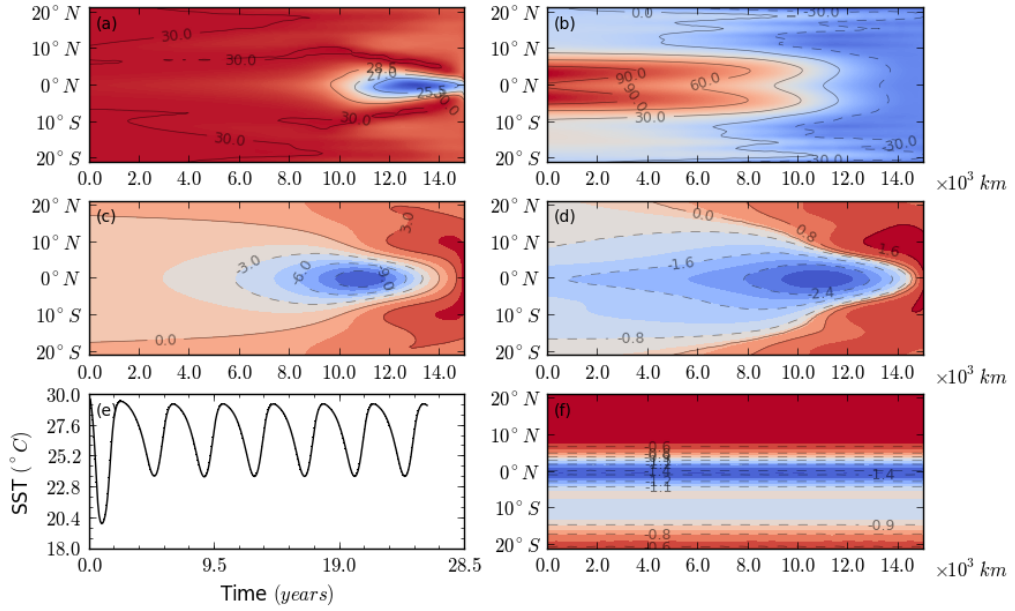
Figure 12: Climatology and variability for TAO/TRITON modeled wind stress with $(G_0, G_1) = (0.2, 0.1)$. (a) The sea-surface temperature (°C) (b) The thermocline depth anomaly compared to a fixed reference level (m) (c) The induced zonal wind speed (m/s) (d) The total zonal wind stress (mPa) (e) Time series of the SST in the *NINO3* region. (f) The external zonal wind stress (mPa)

3.5 Pliocene model fit

Another avenue of interest for this model is to model the external wind stress to existing Pliocene wind fields. During the Pliocene era, 3Ma to 5Ma before present, global temperatures were 2°C - 3°C above present values. Naturally, the Pliocene climate is of great interest because this era opens up a window into the climate we'll face a couple of decades from now.

The HadCM3 PlioMIP Exp 2 experiment ([15]) provides coarse wind fields over the entire globe. Anticipating the results from the off-equatorial wind-stress and TAO fit runs, a different approach is taken. In those runs, the wind stress was spatially averaged in such a way as to lose detailed information about local variations. The model wind fields then show identical spatial distributions and lose comparison value with the original wind field. In an attempt to generate a spatially and numerically similar mean total wind field the original wind stress field is introduced in the model without spatial averaging, but with a scaling factor.

The spherical wind data from HadCM3 was clipped to the box 20°N-20°S and 140°E-80°W. Curvature is neglected, and the data points interpolated on a high resolution grid using a generic curvature minimizing interpolation scheme. Then the grid with the dimensions of the numerical model were overlaid and spatial mean boxes calculated for the corresponding model grid points. Finally, the wind field was converted to a pseudo-stress field using the method outlined
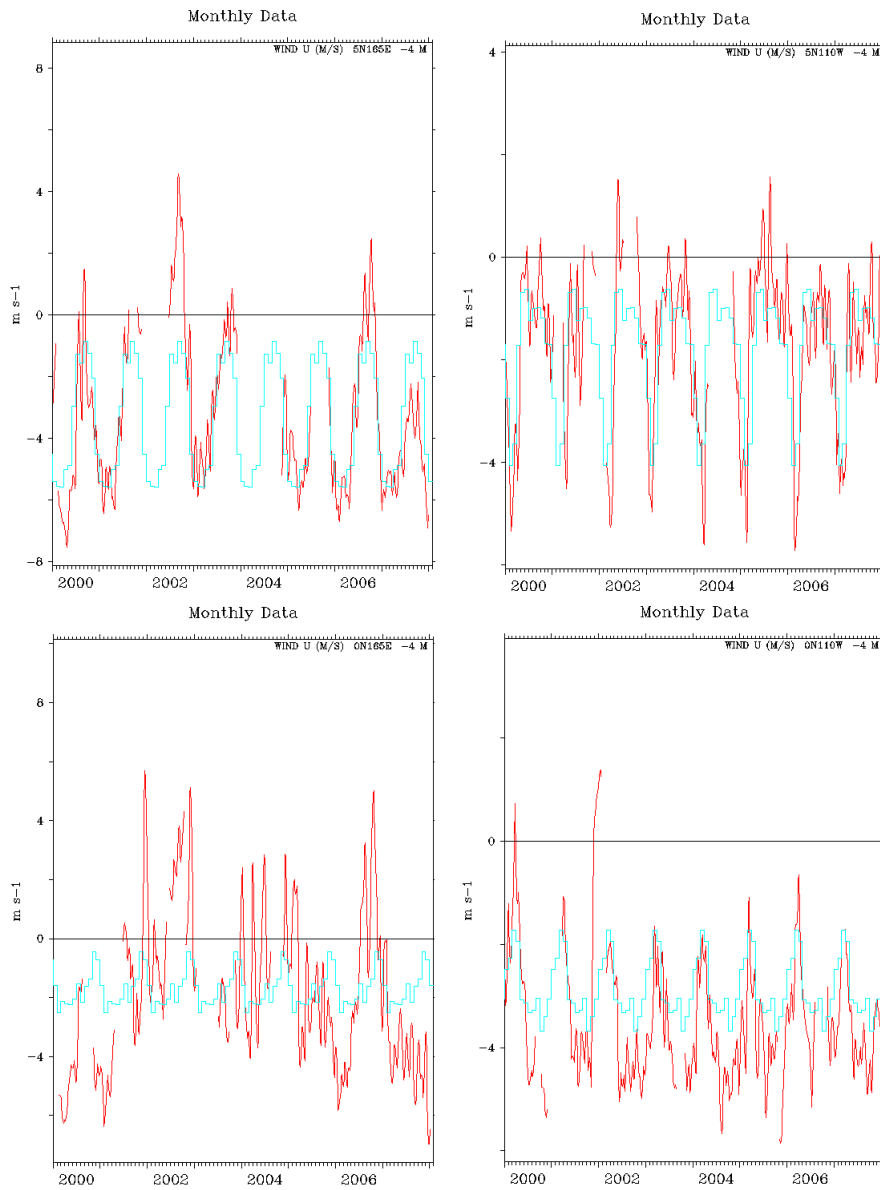
Figure 13: Zonal wind speed (red curves) from the years 2000 to 2008 from four TAO/TRITON buoys. The bottom panel shows the equatorial west and east, respectively, while the top plots show the same longitude but at 5°N. The seasonal cycle with a clear yearly signal is especially evident in the eastern part of the basin.
Courtesy of the TAO Project Office/NOAA/PMEL

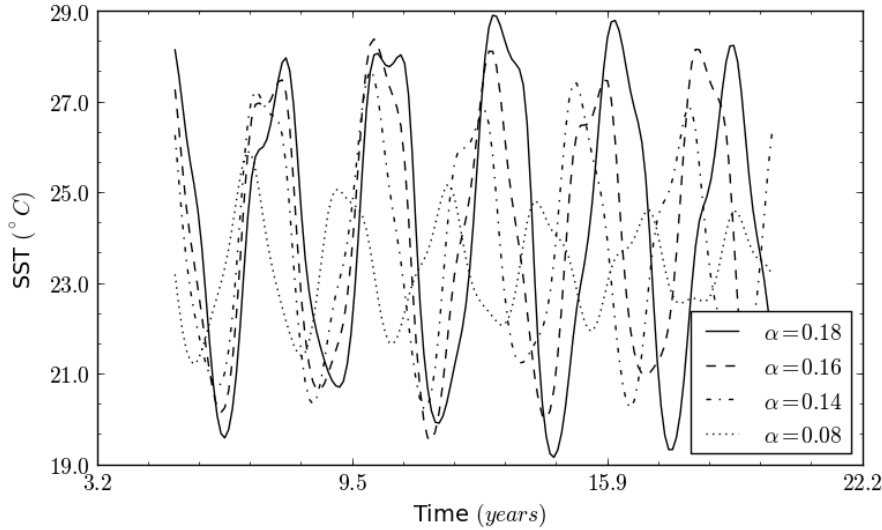earlier, and multiplied by factor τ^* to allow for the de-coupling of the external

Figure 14: Time series of the SST for various temporal forcings of the wind stress. The α parameter determines the amplitude of the temporal variation as defined in eqn 12. $F_0 = 0.5$ in all cases, meaning that the wind stress varied between F_0 and $F_0 - \alpha$ with a period of 1 year. The small drift in periods with different α is due to the shift in mean wind velocities as evidenced by figure 7.

wind stress and the induced internal wind stress. A logarithmically spaced sequence of τ^* in the range $[0.01, 1.0]$ was generated and the output analyzed. Except the wind field the other parameters were identical to the reference case, in particular, the value of T_0 was still set to 30°C despite the higher Pliocene temperature. Figure 16 shows the six runs that resulted in oscillatory behavior. Like with the reference case, there is only one strong mode present, and the sequence of runs shows clear evidence of Hopf-bifurcations. The periods range from 2.8 to 3.3 years, and the position of the CT is entirely consistent with the reference case and shows little variation within the oscillatory domain.

Although the time evolution of the SST looks very similar to the reference case, one notable exception is the case with $\tau^* = 0.100$, where it can be seen that it follows an amplification phase during which the SST oscillations build up in strength, before leveling off. This is probably critical behavior on the boundary of the oscillatory regime, and likely to be seen also in the reference case with the appropriate F_0 value.

Comparing the produced total wind field in panel 17.(d) with the external (HadCM3) wind field in 17.(f) it can be seen that both share similar spatial features and in rough agreement. The τ^* parameterization proved effective in reproducing the external wind field strength and spatial distribution.

In concluding, the model suggests that in the Pliocene a strong El Niño was likely to occur based on the spatial distribution and strength of the zonal wind. Even in weak fields there would form a pronounced CT with a temperature 4°C below T_0. Hence, considering the HadCM3 data it is probable that there was ENSO-like behavior. [1] provides further analysis on the model's results regarding Pliocene conditions.
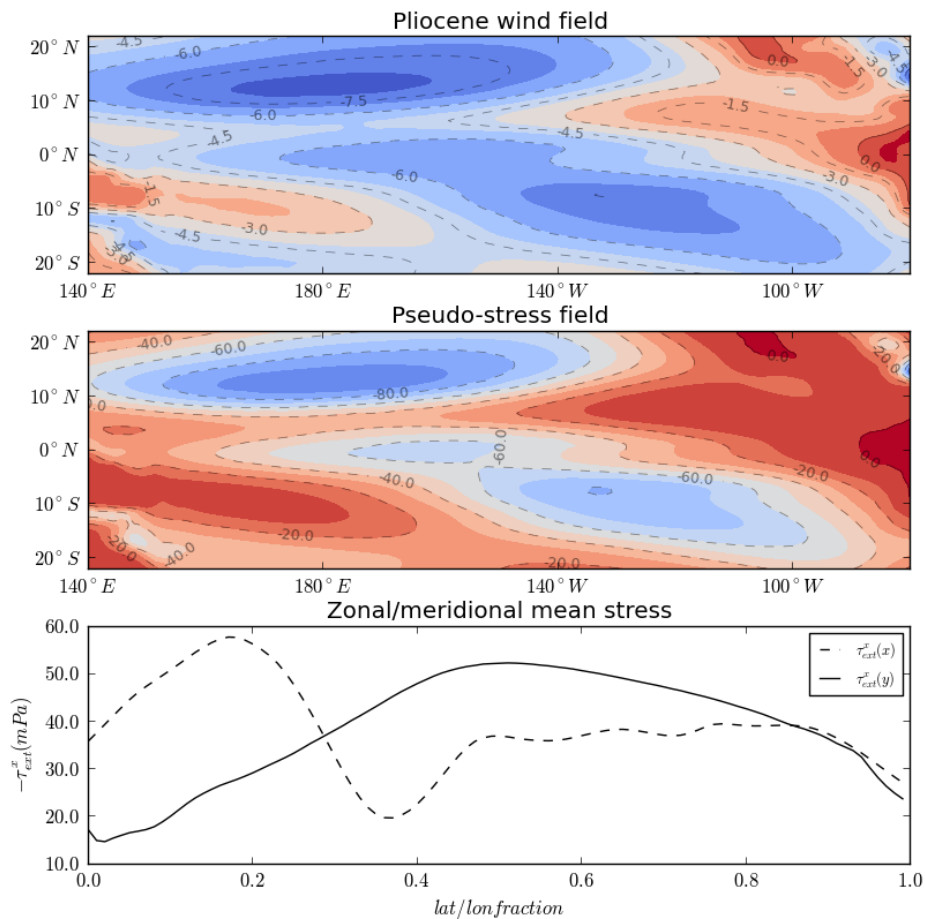
Figure 15: HadCM3 zonal wind data (top) and derived pseudo-stress field (middle) and the zonal and meridional averages (bottom). The solid (dashed) curve shows the zonal (meridional) mean zonal wind stress. The horizontal axis shows the meridional (zonal) extend. The equatorial asymmetries are mirrored with regards to the TAO situation (figure 10), and the wind stress is typically 50% stronger. Remarkably, the wind stress convergence is located in center-west part of the basin.
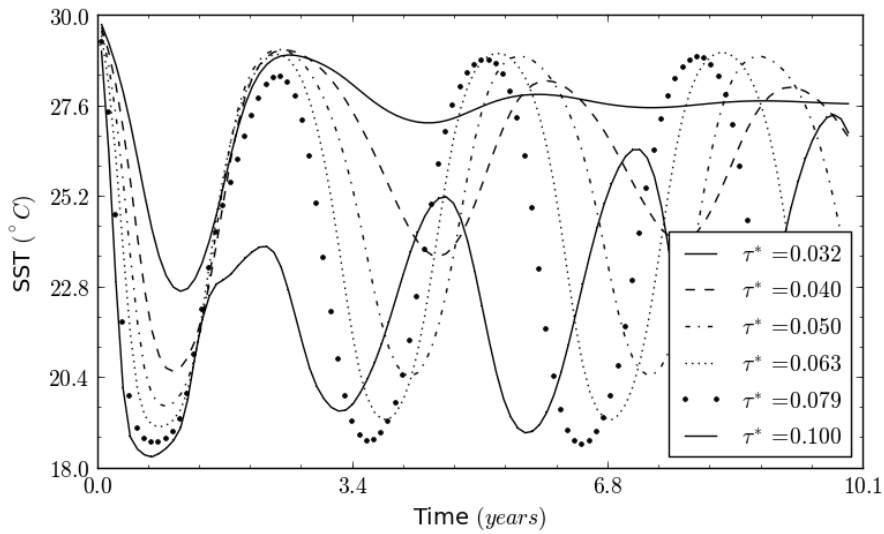
Figure 16: Collage of runs that resulted in stable oscillations. The Pliocene wind field was multiplied by the factor τ^*. The (lower) solid line with $\tau^* = 0.100$ represents the strongest external wind fields able to produce oscillatory behavior. The top solid curve with $\tau^* = 0.032$ marks the smallest value, below which the winds are too weak to sustain oscillations.
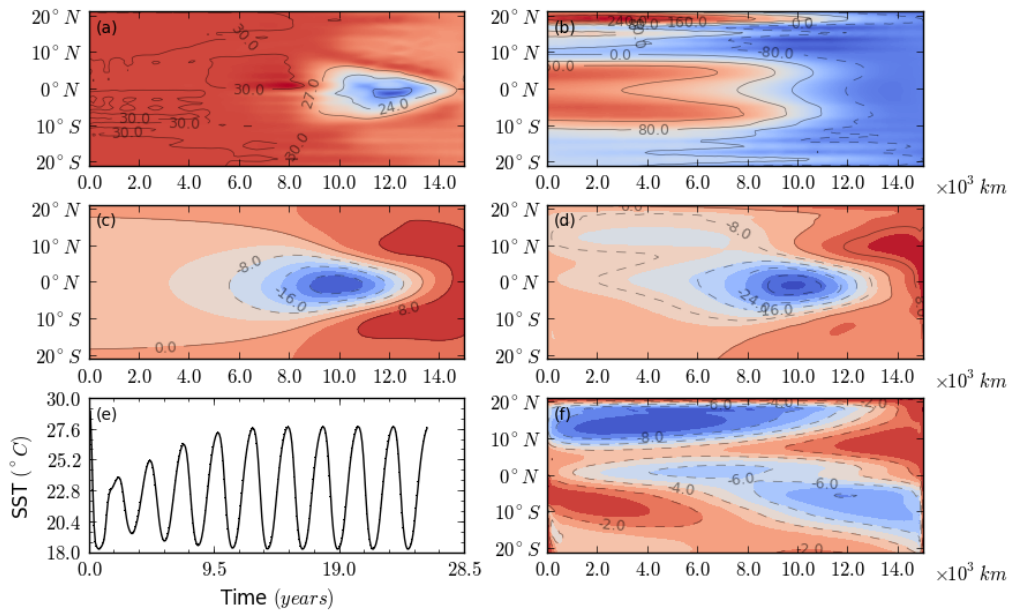

Figure 17: The reference output mean climatology for Pliocene wind data with $\tau^* = 0.100$. (a) The sea-surface temperature (°C) (b) The thermocline depth anomaly compared to a fixed reference level (m) (c) The induced zonal wind speed (m/s) (d) The total zonal wind stress (mPa) (e) Time series of the SST in the *NINO3* region. (f) The external zonal wind stress (mPa)
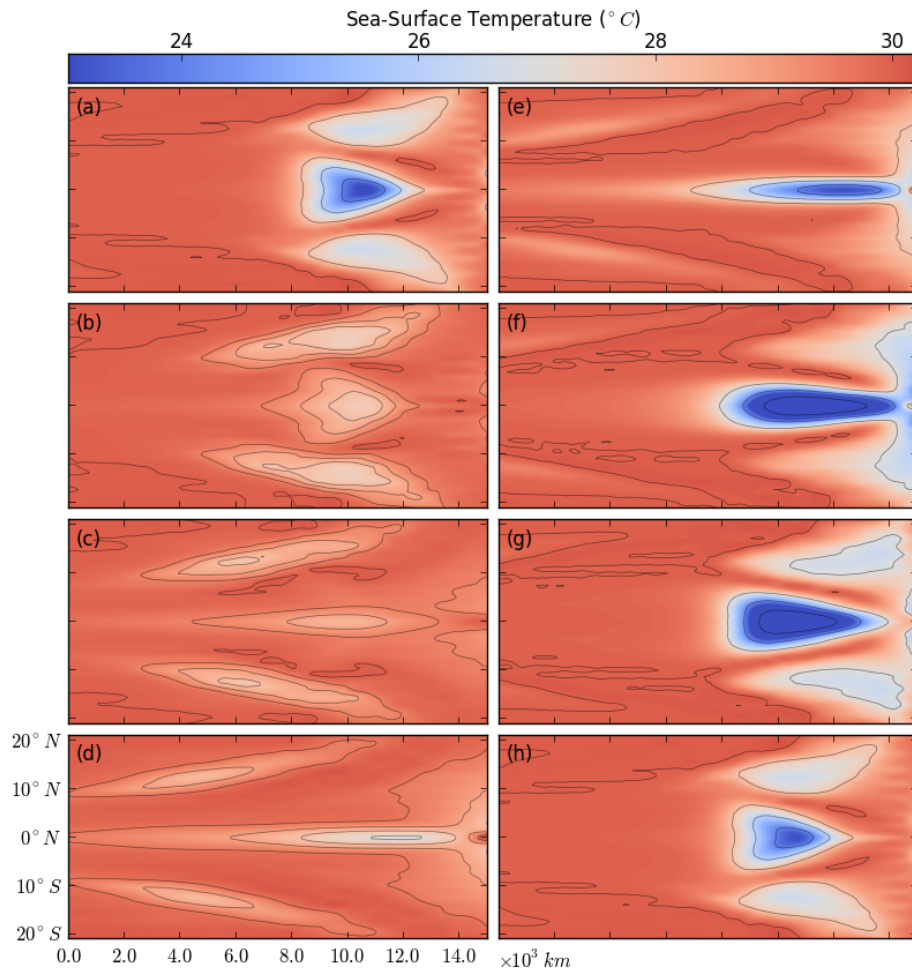
Figure 18: Model output for $(F_0, F_1) = (0.02, 0.04)$ showing the SST during one phase of the oscillation. At $t = 0$ the SST temperature anomaly is 0. The coldest point in the graph reaches 18.9°C . Time units are months since equilibrium SST time, and the time between frames is 6 months. (a) $t = 0$ (b) $t = 6$ (c) $t = 12$ (d) $t = 18$ (e) $t = 24$ (f) $t = 30$ (g) $t = 36$ (h) $t = 42$
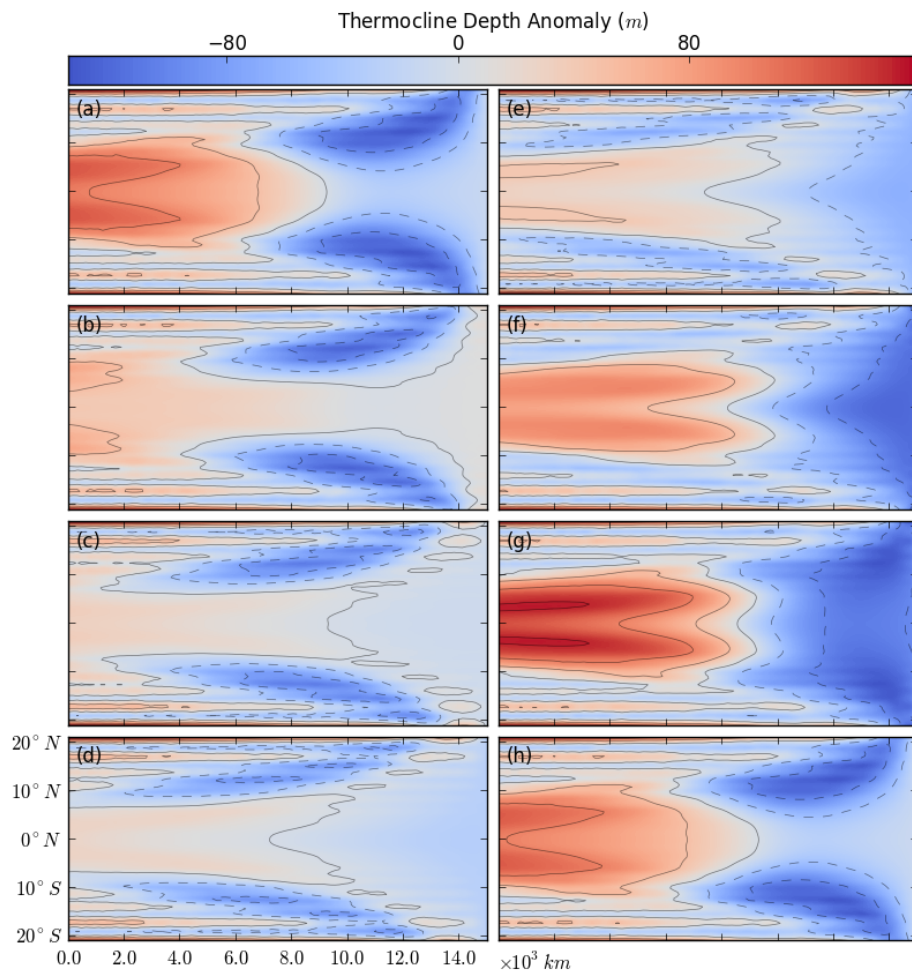
Figure 19: Model output for $(F_0, F_1) = (0.02, 0.04)$ showing the thermocline depth anomaly during one phase of the oscillation. Dotted lines mark negative values. Time units are months since equilibrium SST time, and the time between frames is 6 months. (a) $t = 0$ (b) $t = 6$ (c) $t = 12$ (d) $t = 18$ (e) $t = 24$ (f) $t = 30$ (g) $t = 36$ (h) $t = 42$
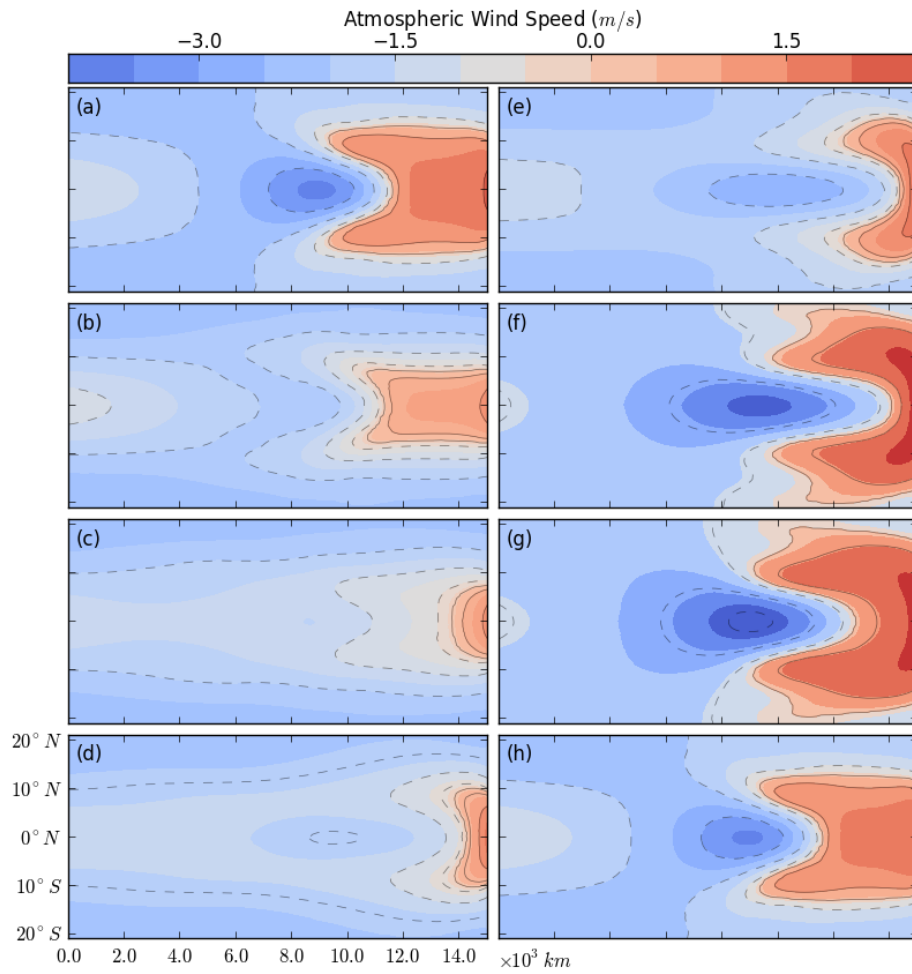
Figure 20: Model output for $(F_0, F_1) = (0.02, 0.04)$ showing the zonal atmospheric wind speed during one phase of the oscillation. Dotted lines mark negative values. Time units are months since equilibrium SST time, and the time between frames is 6 months. (a) $t = 0$ (b) $t = 6$ (c) $t = 12$ (d) $t = 18$ (e) $t = 24$ (f) $t = 30$ (g) $t = 36$ (h) $t = 42$

4   Conclusion

It is well known that within the present climate there exist quasi periodic oscillations in the SST signal of the equatorial Pacific ocean time series. Despite this, modern GCMs have had mixed success in simulating realistic ENSO-like modes ([17], [8]). Specifically, aggregate runs of various GCMs typically show spatial (too far west) and temporal (too short or nonexistent periods) disparities. We've turned to the Zebiak-Cane type ICM to study the behavior of the equatorial Pacific ocean in response to a variety of different wind stress distributions and strengths. Of particular interest is the identification of conditions that show the existence or absence of ENSO-like responses, and how the spatial and temporal characteristics are affected.

The results are compared with a reference case ([2],[1], [3]), which is tuned to reproduce present-day El Niño -like conditions. The reference case has a global wind stress maximum on the equator, and the oscillation commences when the wind stress reaches a critical minimum value, as is well documented in [3]. A similar bifurcation point exists with a purely off-equatorial maximum. Results show a broad range of strengths where the oscillations exist, as long as the wind strength is above and below a critical value. The period of the ENSO is found to be between $3 \sim 4$ years. The spatial extend of the CT shows weak variation with the strength of the equatorial wind stress.

In attempt to provide an alternative, more realistic wind structure, a zonally averaged wind stress of the annual mean TAO wind data is modeled. The prime feature in the TAO data is the off-equatorial positioning of maximum wind stress due to the southerly position of the ITCZ.

With the addition of a simple yearly seasonal cycle the results are also consistent with the reference case, but in general higher wind stresses are required to reach the minimum critical value of the mean wind stress.

The reconstructed Pliocene wind data from the *HadCM3 PlioMIP Exp 2* dataset provides an interesting alternative. Here, the trades are some 50% stronger compared with TAO measurements, and have a bipolar distribution with maximum strength found in the north-western part of the basin. To allow for this information to be retained in the model, the full spatial detail is preserved in the model with a scaling factor. The results are again consistent with the reference case.

We've seen a robust ENSO mode in all simulated conditions. Temporal and spatial details of the external wind stress have little influence on the ΔSST amplitude and period. This suggests that although it is difficult to argue a specific form of the external wind stress in light of the coupled feedbacks, it hardly matters, because if the threshold strength is crossed, ENSO appears.

5 References

[1] A.S. von der Heydt, A.Nnafie, H.A. Dijkstra *Cold Tongue/Warm pool and ENSO dynamics in the Pliocene*, Clim. Past, 2011, doi:10.5194/cp-7-903-2011.

[2] H.A. Dijkstra *The ENSO phenomenon: theory and mechanisms*, Advances in Geosciences, 6, 3-15,2006.

[3] P.C.F. van der Vaart, H.A. Dijkstra *The Pacific Cold Tongue and the ENSO Mode: A Unified Theory within the Zebiak-Cane Model*, AMS,57,2000.

[4] A.E. Gill *Some simple solutions for heat-induced tropical circulation*, Quart. J. R. Met. Soc (1980),106,pp. 447-462

[5] K.M. Lau, S. Yang *Walker Circulation*, 2003 Encyclopedia of Atmospheric Sciences, Elsevier, 2505–2510. doi:10.1006/nwas.2002.0450

[6] J.D. Neelin *On the Interpretation of the Gill Model*, 1989 Journal of Atmospheric sciences, vol 46, no 15

[7] B.C. Roisin, J.M. Beckers *Geophysical fluid dynamics* Elsevier, 2011

[8] P.N. DiNezio et al. *Climate Response of the Equatorial Pacific to Global Warming*, AMS,2009,doi:10.1175/2009JCLI2982.1

[9] G. Burgers, F.F. Jin, G.J. Oldenborgh *The simplest ENSO recharge oscillator*, Geophysical research letters (2005), doi:10.1029

[10] McPhaden, M.J., et al *The Global Tropical Moored Buoy Array*, Proceedings of the "OceanObs'09:Sustained Ocean Observations and Information for Society" Conference (Vol. 2), Venice, Italy, 21-25 September 2009

[11] C. Guan, L. Xie *On the Linear Parameterization of Drag Coefficient over Sea Surface* J. Phys. Oceanogr., 34, 2847–2851. Doi: 10.1175/JPO2664.1

[12] H. Hersbach *Sea Surface Roughness and Drag Coefficient as Functions of Neutral Wind Speed* Journal of Physical Oceanography 41:1, 247-251

[13] Kara, A. Birol, Alan J. Wallcraft, E. Joseph Metzger, Harley E. Hurlburt, Chris W. Fairall *Wind Stress Drag Coefficient over the Global Ocean* AMS Volume 20, Issue 23 (December 2007)

[14] P.S. Schopf, M.J. Suarez *Ocean wave dynamics and the timescale of ENSO* Journal of Physical Oceanography 20:1, 629-645 (1990)

[15] Haywood et al. *Large scale features of Pliocene climate in CP.*

[16] S.E. Zebiak, M.A. Cane *A model El Niño -Southern Oscillation* Mon. Weather Rev., 115, 2262-2278, (1987)

[17] J.L. Lin *Interdecadal variability of ENSO in 21 IPCC AR4 coupled GCMs.*, Geophysical research letters, vol 34, 2007 doi:10.1029/2006GL028937

A Model of the ocean

This appendix describes briefly the steps to arrive at the central equations governing the oceanic and atmospheric dynamics from the generalized Navier-Stokes equations. Although there are many text books that deal with this derivation in detail (see [7]), I've found it helpful in highlighting the approximations and assumptions underpinning the model.

A.1 The shallow-water ocean

Recall the generalized Navier-Stokes,

$$\frac{\mathrm{d}\vec{u}}{\mathrm{d}t} - 2\vec{\Omega} \times \vec{u} = -\frac{1}{\rho}\nabla p + \nu\nabla^2\vec{u} + \vec{f} \tag{13a}$$

$$\frac{\partial \rho}{\partial t} + \nabla \cdot (\rho\vec{u}) = 0 \tag{13b}$$

$$\frac{\mathrm{d}}{\mathrm{d}t} = \frac{\partial}{\partial t} + \vec{u} \cdot \nabla \tag{13c}$$

where the $\vec{\Omega}$ term in the momentum balance represents the Coriolis force, followed by the the continuity equation. The last equation is the material derivative. With the following assumptions,

(A.1) Metric terms due to the curvature of the Earth have been dropped.
(A.2) Constant gravitational field g and no tidal effects
(A.3) Incompressibility, constant ρ
(A.4) Equatorial beta-plane approximation $f_0 \approx 0$
(A.5) Friction dominated by Reynold-stresses
(A.6) Small aspect ratio:
    (A.6a) Hydrostatic equilibrium dominates vertical acceleration
    (A.6b) Reynold stress can be split in horizon component μ_H and vertical component μ_V

The equations (13) can be simplified. Near the equator, where the Coriolis parameter is zero, the general curvilinear coordinates (x, y, z) with x pointing eastward, y northwards, and z upwards, will form a special plane called the beta-plane, where the coriolis force takes on an approximately linear form. The fluid momentum balance becomes,

$$\frac{\mathrm{d}u}{\mathrm{d}t} - \beta_0 y v = -\frac{1}{\rho}\frac{\partial p}{\partial x} + \mu_H\left(\frac{\partial^2 u}{\partial x^2} + \frac{\partial^2 u}{\partial y^2}\right) + \mu_V\frac{\partial^2 u}{\partial z^2} \tag{14a}$$

$$\frac{\mathrm{d}v}{\mathrm{d}t} + \beta_0 y u = -\frac{1}{\rho}\frac{\partial p}{\partial y} + \mu_H\left(\frac{\partial^2 v}{\partial x^2} + \frac{\partial^2 v}{\partial y^2}\right) + \mu_V\frac{\partial^2 v}{\partial z^2} \tag{14b}$$

$$0 = -\frac{1}{\rho}\frac{\partial p}{\partial z} - g \tag{14c}$$

to be combined with the continuity equation,

$$\frac{\partial u}{\partial x} + \frac{\partial v}{\partial y} + \frac{\partial w}{\partial z} = 0 \tag{15}$$

The set of equations (14) and (15) are subject to mixed boundary conditions at the ocean-atmosphere interface at $z = \eta$,

$$p = p_a \tag{16a}$$

$$\rho\mu_V \frac{\partial u}{\partial z} = \tau_x \tag{16b}$$

$$\rho\mu_V \frac{\partial v}{\partial z} = \tau_y \tag{16c}$$

Here p_a is the atmospheric pressure at sea level and $\vec{\tau}$ is the wind stress. μ_H and μ_V are the coefficients that determine the strength of horizontal and vertical momentum mixing.

The flow is confined by the material interface that separates the ocean from the atmosphere, hence the normal flow component vanishes,

$$\vec{u} \cdot \nabla(z - \eta(t, x, y)) = 0 \tag{17}$$

where $z = \eta(t, x, y)$ is the elevation of the interface. We presume the bottom to be flat, and η becomes the depth of the fluid column. It can be re-written as the dynamic boundary condition,

$$\frac{\mathrm{d}(z - \eta(t, x, y))}{\mathrm{d}t} = 0 \tag{18}$$

A.2   The shallow-water layered ocean

The last refinement to complete the ocean model is to introduce a second layer representing the deep ocean. This has the conceptual benefit of redressing the top layer as being generally well-mixed and juxtaposed on the immobile deep ocean of greater density $\rho + \Delta\rho$. It also has the added benefit of being able to induct the boundary conditions (18),(16) into the volume differential equations (14) and (15) by performing an integration over the fluid depth.

Let the layer interface be prescribed as $z - \zeta(t, x, y) = 0$, so that the top layer thickness becomes $h(t, x, y) = \eta(t, x, y) - \zeta(t, x, y)$. Then the same equations stated earlier apply, except for the following modifications,

$$\frac{\partial p_2}{\partial z} = -(\rho + \Delta\rho)g \tag{19a}$$

$$p_1 = p_2|_{z=\zeta} \tag{19b}$$

$$\frac{\mathrm{d}(z - \zeta)}{\mathrm{d}t}\Big|_{z=\zeta} = 0 \tag{19c}$$

The model completes by integrating (14) and (15) over the top layer,

$$\int_{z=\zeta}^{z=\eta} \ldots \, dz = 0$$

Removing the terms involving explicit z-dependence, and collecting the remaining terms under the integral.

For example, for the vertical momentum mixing term μ_V simplifies as,

$$\int_{z=\zeta}^{z=\eta} \mu_V \frac{\partial^2 u}{\partial z^2}\, dz = \mu_V \frac{\partial u}{\partial z}\bigg|_{z=\zeta}^{z=\eta}$$

$$= \frac{\tau_x}{\rho} - 0$$

$$\int_{z=\zeta}^{z=\eta} \frac{\tau_x}{h\rho}\, dz = \frac{\tau_x}{\rho}$$

Likewise for z-component of the convective terms for u and v (shown only for u),

$$\int_{z=\zeta}^{z=\eta} \left(w\frac{\partial u}{\partial z} + u\frac{\partial w}{\partial z} \right) dz = wu|_{z=\zeta}^{z=\eta}$$

$$= 0$$

Since the continuity equation does not fully determine the relationship between w and u, the identity must hold for both terms, and both terms identically vanish. Furthermore, the pressure term can be written in terms of h by averaging over the top layer using the following procedure, where care must be taken to handle the density discontinuity (at $z = 0$),

$$\int_{-\epsilon}^{\epsilon} \frac{\partial p}{\partial z} dz = \int_0^{\epsilon} \frac{\partial p_1}{\partial z} dz + \int_{-\epsilon}^0 \frac{\partial p_2}{\partial z} dz$$

$$= p_1(\epsilon) - p_2(-\epsilon)$$

$$\int_{-\epsilon}^{\epsilon} \rho g dz = \int_0^{\epsilon} \rho g dz + \int_{-\epsilon}^0 (\rho + \Delta\rho) g dz$$

$$= \Delta\rho g \epsilon$$

here p_1 and p_2 represent the pressures in the top and bottom layer. Use has been made of continuity across the 1,2 layer interface in the second step. By letting $\epsilon \to h$ and switching back to the original coordinates we get,

$$\frac{\partial}{\partial x} \int_{z=\zeta}^{z=\eta} \frac{\partial p}{\partial z} dz = \frac{\partial}{\partial x} \int_{z=\zeta}^{z=\eta} \Delta\rho g\, dz$$

$$= \Delta\rho g \frac{\partial h}{\partial x}$$

Substituting these expressions in the integration terms, and collecting terms under the integral again results in the final equations,

$$\frac{\partial u}{\partial t} + u\frac{\partial u}{\partial x} + v\frac{\partial u}{\partial y} - \beta_0 y v = -g'\frac{\partial h}{\partial x} + \frac{\tau_x}{h\rho} \qquad (20\text{a})$$

$$\frac{\partial v}{\partial t} + u\frac{\partial v}{\partial x} + v\frac{\partial v}{\partial y} + \beta_0 y u = -g'\frac{\partial h}{\partial y} + \frac{\tau_y}{h\rho} \qquad (20\text{b})$$

$$\frac{\partial h}{\partial t} + \frac{\partial(uh)}{\partial x} + \frac{\partial(vh)}{\partial y} = 0 \qquad (20\text{c})$$

with $g' = g\Delta\rho/\rho$, and friction terms have been dropped. These are the shallow water equations on the equatorial beta-plane.